A Novel RPCA Method Using Log-Weighted Nuclear and $L_{2,1}$ Norms Combined with Contrast-Limited Adaptive Histogram Equalization (CLAHE) for High Dimensional Natural and Medical Image Data

Habte Tadesse LIKASSA[1], Ding Geng Chen[1,3,*] and Dayu Sun[2]

[1]*Department of Biostatistics, College of Health Solutions, Arizona State University, Phoenix, AZ 85004, USA*

[2]*Department of Biostatistics and Health Data Science, School of Medicine, Indiana University, Indianapolis, IN, 46202, USA*

[3]*Department of Statistics, University of Pretoria, South Africa*

Abstract: Estimating the true underlying images from distorted high-dimensional data is crucial for applications in high-profile fields such as crime detection in security, clinical settings and medical diagnosis in healthcare, and radar imaging in signal processing. Existing statistical methods often struggle with robustness and image reconstruction quality when processing high-dimensional image data. While Robust Principal Component Analysis (RPCA) is widely used for image recovery, its reliance on uniform weights with singular value decomposition (SVD) weakens performance, especially in noisy environments. The L_1 norm also fails to capture image details and recovery under high noise levels, a critical limitation for applications like medical diagnoses, where detail is essential. These challenges emphasize the need for improved methods to handle noise and enhance image quality in sensitive fields. Therefore, this paper proposes a novel RPCA method that integrates CLAHE with Log weighted nuclear norm (LWNN) and the $L_{2,1}$ norm for high-dimensional natural and medical imaging. To reduce the computational load, our novel method is formulated into a new optimization problem and solved using the Alternating Direction Method of Multipliers (ADMM). This method leverages LWNN for enhanced low-rank approximation to drastically prune out the anomalies in images and the $L_{2,1}$ norm for improved sparse component recovery. Our approach has superior performance in image reconstruction compared to other state-of-the-art methods (SOTAs), showing significant advancements with real-world datasets. An interesting finding of this research is that combining the LWNN with the $L_{2,1}$ norm is highly effective at removing noise from images. Furthermore, when the CLAHE technique is combined with LWNN and the $L_{2,1}$ norm, it significantly enhances the extraction of previously unseen features, making blood vessels in medical images much clearer and more distinguishable. This combination proves to be a powerful approach for medical image analysis, revealing details that are otherwise difficult to detect. This method will be used for crime detection in security intelligence, and clinical settings and medical diagnosis in human retinal eyes.

Keyword: RPCA, Low-rank, Computational statistics, Medical Data, CLAHE, LWNN + $L_{2,1}$ Norm.

INTRODUCTION

In computational statistics, RPCA is a powerful statistical method in high-dimensional image recovery [2, 10-12], widely used for decomposing data into low-rank and sparse components. This decomposition is crucial in diverse applications such as image alignment [26], anomaly detection for security purposes [7], video background subtraction [24], medical image analysis [6, 16-18], and retinal image enhancement [10]. RPCA also finds significant utility in tasks like image denoising [21] and image classification [28]. By isolating the underlying low-rank structure from high dimensional images influenced with noise and outliers [4, 30], RPCA plays a central role in accurate image recovery data analysis from high-dimensional image data [3, 14, 29]. However, these methods lack to be computationally efficient.

To estimate the true underlying object from a distorted high dimensional images, the pioneering RPCA framework by [2] is formulated as:

$$\min_{\mathbb{L},\mathbb{S}} \|\mathbb{L}\|_* + \lambda\|\mathbb{S}\|_1 \;\; !\mathrm{S.t}\;\; \mathbb{M} = \mathbb{L} + \mathbb{S} \quad (1)$$

Where $\|\mathbb{L}\|_*$ represents the nuclear norm of the matrix $\mathbb{L}$ (the sum of its singular values), $\|\mathbb{S}\|_*$ is the ℓ_1-norm of the matrix $\mathbb{S}$ (the sum of the absolute values of its entries). The regularization parameter $\lambda\,!\;\;0$ balances the contributions of the low-rank matrix L and the sparse matrix $\mathbb{S}$.

Since the groundbreaking work on RPCA by Candés *et al*. (2011) [2], a wide array of methods has emerged for robust sparse low-rank image recovery[31]. Pluim *et al* (2003) [20] introduced a novel technique for mutual information based registration of medical images for measuring image similarity. Peng *et al*. (2012) [19] proposed a robust image recovery method to address misalignment issues, but its performance is limited as all images are compressed with the same SVD, reducing its adaptability. To enhance the performance, a new method was introduced by [8], utilizing geometric transformations. However, the technique struggles when noise levels are excessively high. Lui *et al*. (2022) [14] proposed RPCA with low-rank matrix recovery (RPCA-LRMR),

*Address correspondence to this author at the Department of Biostatistics, College of Health Solutions, Arizona State University, Phoenix, AZ 85004, USA; E-mail: dinchen@asu.edu

leveraging local smoothness for image recovery. This approach uses the correlated total variation norm minimization problem. However, this reliance on local features limits its versatility. Similarly, Liu et al. (2018) [13] introduced RPCA with $L_0 - L_1$ regularization (RPCA-NNM), where the L_0 norm addresses sparse outliers and the L_1 norm tackles additive noise. While this method enhances image quality, it still struggles to deliver significant performance improvements. Likassa *et al*. (2024) [10] developed an enhanced RPCA with weighted nuclear norm and Affine transformation (RPCA-WAT) for medical image recovery. This method uses the weighted nuclear norm to minimize errors and the $L_{2,1}$ norm to filter out noise. Despite its strengths, this method lacks the capability to effectively recover intricate image details. This limitation in capturing and detailing certain characteristics during medical image analysis may restrict its applicability in clinical settings and medical diagnosis. Rajpurohit *et al*. (2024) [23], a Block Minorization-Maximization Method for Row-Sparse Principal Component Analysis (BM2A) was introduced, offering enhanced image reconstruction by effectively addressing row-sparsity and improving recovery accuracy compared to traditional RPCA methods. Moreover, the block minorization-maximization (MM) algorithm may suffer from slow convergence, the risk of converging to local optima, dependence on the initial solution, and high computational cost, especially if the subproblems are complex or poorly partitioned. Furthermore, a log weighted and $L_{2,1}$ norms has been suggested for enhanced image recovery [5]. Despite these improvements, existing methods still exhibit insufficient robustness, as optimizing weight adjustments remains critical for more accurate recovery of image structures. The deep learning [1, 9] is though good for image reconstruction, however they require more datasets which undermines the computational loading.

Existing RPCA methods face significant challenges when applied to high-dimensional medical images. They struggle to handle noise, variations, and occlusions effectively. These limitations make them less robust for clinical and medical diagnoses. A key issue is their reliance on SVD, which treats the entire image as having the same singular values. This approach is not realistic as it fails to capture the detailed characteristics of the image. As a result, it does not effectively reveal hidden underlying features such as background extractions or clearly highlight structures like blood vessels.

This paper proposes a novel RPCA method that integrates LWNN and the $L_{2,1}$ norm for better image recovery. LWNN reduces noise by adjusting singular values, while the $L_{2,1}$ norm potentially captures the issue of outliers and variations, offering more accurate image reconstruction in challenging conditions.

The major contributions of this paper are:

- We propose a novel RPCA model integrating LWNN for improved image recovery data analysis, effectively weighting and truncating singular values to enhance noise robustness and preserve low-rank features. Incorporating the log-weighted nuclear norm enhances low-rank recovery, noise suppression, and robustness compared to the traditional weighted nuclear norm in matrix tasks.
- To enhance robustness against noise and outliers, we also incorporate the $L_{2,1}$ norm into RPCA to remove correlated samples in high-dimensional images.
- By incorporating CLAHE, our method accurately extracts the underlying object and background, improving image decomposition and reducing noise sensitivity.
- To reduce the computational load, our method introduces LWNN, solved via ADMM, achieving significant performance gains over traditional methods.
- The combination of CLAHE and LWNN marks a major advancement over existing RPCA techniques, outperforming recent SOTAs.

The structure of this paper is organized as follows. The problem formulation is described in Section 2. The datasets described in Section 3 and the simulation results are given in Section 4. Finally, discussions and conclusions are given in Section 5.

2. PROBLEM FORMULATION

Given an observed matrix $\mathbb{M} \in \mathbb{R}^{m \times n}$ where m is obtained from pixels and n is number of images, RPCA aims to decompose $\mathbb{M}$ into a low-rank matrix $\mathbb{L}$ and a sparse matrix $\mathbb{S}$, such that:

$$\mathbb{M} = \mathbb{L} + \mathbb{S} \tag{2}$$

The optimization problem in Eqn. 1 has a significant drawback: it assigns equal weights to all images. To address this limitation, we introduce the LWNN, defined as follows:

$$\min_{\mathrm{L,S}} \left\{ \sum_{i=1}^{r} \log\left(1 + \frac{\sigma_i(\mathrm{L})}{\lambda}\right) + \lambda \|\mathbb{S}\|_1 \right\} \quad \mathrm{S.t.}\ \mathbb{M} = \mathbb{L} + \mathbb{S} \tag{3}$$

To mitigate the influence of correlated samples, the $L_{2,1}$ norm was proposed as an improvement over the L_1 norm as in [12]. The L_1 norm still struggles with robustness, as it imposes uniform sparsity across all groups of images, which can be overly restrictive. To enhance the robustness and resilience of the method against noise and outliers, we considered the $L_{2,1}$ norm over the L_1 norm as in [10], and log weighted nuclear norm as in [15]. This leads to a new and improved optimization problem, formulated as follows:

$$\min_{\mathrm{L,S}} \left\{ \sum_{i=1}^{r} \log\left(1 + \frac{\sigma_i(\mathrm{L})}{\lambda}\right) + \lambda \|\mathbb{S}\|_{2,1} \right\} \quad (4)$$
$$!\,.\,\mathrm{t}.\,\mathbb{M} = \mathbb{L} + \mathbb{S}$$

where $\mathbb{L} \in \mathbb{R}^{m\times n}$ is the low-rank matrix, $\mathbb{S} \in \mathbb{R}^{m\times n}$ is the sparse matrix, $\sigma_i(\mathbb{L})$ denotes the i^{th} singular value of $\mathbb{L}$, and $\|X\|_{2,1} = \sum_{i=1}^{m} \sqrt{\sum_{j=1}^{n} X_{i,j}^2}$, $log(\cdot)$ is the natural logarithm function. The summation is taken over all rows i of the matrix $\mathbb{S}$. This optimization problem for RPCA with a log-based weighted nuclear norm along with the CLAHE can be expressed as:

$$\begin{aligned} &\min_{\mathrm{L,S}} \left\{ \|\mathbb{L}\|_{log} + \lambda \|\mathbb{S}\|_{2,1} \right\} \\ !\quad &\mathrm{S.t.}\, \mathbb{M}_{\mathbb{CLAHE}} = \mathbb{L} + \mathbb{S} \end{aligned} \quad (5)$$

where $\|\mathbb{L}\|_{log}$ is represented by $\sum_{i=1}^{r} log\left(1 + \frac{\sigma_i(\mathbb{L})}{\lambda}\right)$, r is representing the truncation level, it is noted that the $\|\mathbb{L}\|_{2,1}$ can measure the columnwise sparsity more accurately than the $L_{2,1}$ norm if contains larger values.

2.1. Proposed Method

To solve an optimization problem, we used an ADMM approach as in [12]. Then, when we apply the ADMM approach to Eqn. 5, which is given by:

$$\begin{aligned} \mathcal{L}(\mathbb{L}, \mathbb{S}, , \boldsymbol{\Gamma}) = \|\mathbb{L}\|_{log} + \lambda \|\mathbb{S}\|_{2,1} + \langle \boldsymbol{\Gamma}, \mathbb{M}_{\mathbb{CLAHE}} - \mathbb{L} - \mathbb{S} \rangle \\ + \frac{\mu}{!} \|\mathbb{M}_{\mathbb{CLAHE}} - \mathbb{L} - \mathbb{S}\|_F^2 \end{aligned} \quad (6)$$

where $\boldsymbol{\Gamma}$! $\Re^{m\times n}$ denotes that the Lagrangian multiplier, μ is denoting the penalty parameter. Then, considering the relationship between the Frobenious and cross product, then Eqn (6) can be further modified to first we need to find the optimal parameter corresponding to $\mathbb{L}$ so that we can get

$$\begin{aligned} \mathbb{L}^{!\,k+1)} = \underset{\mathbb{L}}{\mathrm{argmin}} \mathcal{L}\{\|\mathbb{L}\|_{log} + \frac{\mu^{(k)}}{2} || \mathbb{M}_{\mathbb{CLAHE}}{}^{(k)} - \mathbb{L} \\ ! \quad -\mathbb{S}^{(k)} + \frac{\boldsymbol{\Gamma}^{(k)}}{\mu^{(k)}} ||_F^2 \} \end{aligned} \quad (7)$$

To find the optimal parameter of $\mathbb{L}$ as in [27], consider two matrices $\mathbb{X} \in \Re^{r\times m}$, $\mathbb{Y} \in \Re^{r\times m}$ and $\mathbb{X}!\,^T = \mathbb{I}, \mathbb{Y}\mathbb{Y}^T = \mathbb{I}$. Then, the LWNN can redefined as

$$\|\mathbb{L}\|_{t,w} = \|\mathbb{L}\|_{W,*} - \arg \min_{\mathbb{X}\mathbb{X}^T=\mathbb{I}, \mathbb{Y}\mathbb{Y}^T=\mathbb{I}} \mathrm{tr}(\mathbb{X}\mathbb{L}\mathbb{Y}^T) \quad (8)$$

where $\mathbb{I}$ is an identity matrix. When $\mathbb{X} = [\boldsymbol{u}_1 \ldots \boldsymbol{u}_r]^T$ and $\mathbb{Y} = [\boldsymbol{v}_1 \ldots v_r!^T$, $\mathrm{tr}(\mathbb{X}\mathbb{L}\mathbb{Y}^T)$ can achieve its maximum value. Then, Eq. 8 can be rewritten as

$$\begin{aligned} \min_{\mathrm{L,S}} \|\mathbb{L}\|_{tr} - \min_{\mathbb{X}=\mathbb{Y}} \mathrm{tr}(\mathbb{X}\mathbb{L}\mathbb{Y}^T) + \lambda \|\mathbb{S}\|_{2,1} \\ \mathrm{s.t.}\, \mathbb{M}_{\mathbb{CLAHE}} = \mathbb{L} + \mathbb{S} \end{aligned} \quad (9)$$

To solve Eq. 9, we employ the ADMM scheme again. Then setting $L_0 = 0$ as initialization, in the l^{th} iteration we compute the SVD of L_l to obtain U_r and V_r, then update L_{l+1} and S_{L+1} by solving the following optimization problem on the use of U_r and $V_!$

$$\begin{aligned} \min_{\mathbb{L},\mathbb{S}} \|\mathbb{L}\|_{*,w} - \mathrm{tr}(\mathbb{U}_r^T \mathbb{L} \mathbb{V}_r) + \lambda \|\mathbb{S}\|_{2,1} \\ ! \qquad \mathrm{s.t.}\, \mathbb{M}_{!\,\mathbb{LAHE}} = \mathbb{L} + \mathbb{S} \end{aligned} \quad (10)$$

The above equation can be reduced to the following form

$$\begin{aligned} \mathcal{L}(\mathbb{L}!\mathbb{S}, Y, \mu) = \|\mathbb{L}\|_{t,w} - \mathrm{tr}(U_r^T \mathbb{L} V_r) + \lambda \|\mathbb{S}\|_{2,1} \\ + \langle Y, \mathbb{M}_{\mathbb{CLAHE}} - \mathbb{L} - \mathbb{S} \rangle + \frac{\mu}{2} \|M_{\mathrm{CLAHE}} - L - S\|_F^2 \end{aligned} \quad (11)$$

By applying singular value shrinkage operator on Eq. 11, then we can get:

$$\begin{aligned} \mathbb{L}_{k+1} = \mathbb{D}_{\mu_k^{-1}} \left\{ \begin{array}{c} \mathbb{M}_{CLAHE} - \\ \mathbb{S}_{k+1} ! \ \mu_k^{-1}(\mathbb{Y}_k + \mathbb{U}_{r,k} \mathbb{Y}_{r,k}^T) \end{array} \right\} \\ ! \qquad ! \qquad ! \quad ! \quad = \mathbb{U} \mathbb{S}_{\boldsymbol{\mu k}}^{-1} \hat{\Sigma} \mathbb{V}^T \end{aligned} \quad (12)$$

where $\mathbb{U}$, $\hat{\Sigma}$ and $\mathbb{V}$ are obtained by tw SVD of $M_{\mathrm{CLAHE}} - \mathbb{S}_{k+1} + \mu_k^{-1}(\mathbb{Y}_! + U_{r,k}, \mathbb{V}_{r,k}^T)$ where $\mathbb{U} = (\boldsymbol{u}_1 \ldots \boldsymbol{u}_m) \in \Re^{m\times n}$ and $\mathbb{V} = (\boldsymbol{v}_1 \ldots \boldsymbol{v}_n) \in \Re^{n\times n}$, and $\hat{\Sigma}$ is the diagonal matrix with the thresholded singular values obtained after taking the log-weighted thresholding on the singular values $\sigma_!$.

Secondly, to update $\mathbb{S}$, we keep $\mathbb{L}$ and Γ as constants, so $\mathbb{S}^{(k+1)}$ can be determined by

$$\mathbb{S}^{(k+1)} = \underset{\mathbb{S}}{\mathrm{argmin}} \mathcal{L}\left\{\mathbb{L}^{(k+1)}, \mathbb{S}, \Gamma\right\} \quad (13)$$

Again, by ignoring all irrelevant terms of S, Eq. (13) can be simplified as

$$\begin{aligned} \mathbb{S}^{(k+1)} = \underset{!}{\mathrm{argmin}} \{\lambda \|\mathbb{S}\|_{2,1} + \frac{\mu^{(k)}}{2} || \mathbb{M}_{\mathbb{CLAHE}} - \mathbb{L}^{(k)} \\ -\mathbb{S} + \frac{\boldsymbol{\Gamma}^{(k)}}{\mu^{(k)}} ||_F^2 \} \end{aligned} \quad (14)$$

Invoking the augmented Lagrangian multiplier and the soft shrinkage operator as in [10], by considering lemma as in [12], the update of the i^{th} column of $\mathbb{S}^{(k+1)}$, $\mathbb{S}_i^{(k+!)}$ is given by

$$!\ {}_i^{(k+1)} = \begin{cases} \dfrac{\left\|v_i^{(k)}\right\|_2 - \frac{\lambda^{(k)}}{\mu^{(k)}}}{\left\|v_i^{(k)}\right\|_2} !\ {}_i^{(k)}, & \text{if} \left\|\boldsymbol{U}_i^{(k)}\right\|_2 \geq \frac{\lambda^{(k)}}{\mu^{(k)}} \\ 0, & \text{otherwise} \end{cases} \quad (15)$$

where $\boldsymbol{U}^{(k)} = \{\mathbb{M}_{\mathbb{CLAHE}} - \mathbb{L}^{(k)} - \mathbb{S} + \frac{\boldsymbol{\Gamma}^{(k)}}{\mu^{(k)}}\}$.

Following the same steps, the Lagrangian multiplier Γ is updated by

$$\Gamma^{(k+1)} = \Gamma^{(k)} + \mu^{(k+1)}\{M_{CLAHE}^{(k)} - \mathbb{L}^{(k+1)} - \mathbb{S}^{(k+1)}\} \quad (16)$$

Likewise, updated parameters, the regularization parameter μ is updated by

$$\mu^{(k+1)} !\ \ min\left\{\mu\mu_{max}, \rho\mu^{(k)}\right\} \quad (17)$$

The performance of the proposed method is evaluated through visualization and numerical simulations, utilizing the Peak Signal-to-Noise Ratio (PSNR), Structural Similarity Index (SSIM), and Relative Absolute Error (RAE). Higher performance is indicated by lower PSNR and SSIM values between the corrupted and recovered images, while a higher RAE suggests better recovery of distorted images. This means that a lower PSNR and SSIM between the degraded and recovered images using the proposed method, along with a higher RAE, indicate that the recovered images are closer to the ground truth. This suggests that the proposed method has greater potential in recovering degraded images compared to SOTA methods. For PSNR and SSIM, higher values between the ground truth and enhanced images indicate better performance, while for RAE, lower values signify better performance of the method.

3. DATASETS

This section describes various natural complicated images and medical image datasets to evaluate the performance of the new method described in Section 2. In this research, we considered two distinct datasets: The first comprises complicated natural images, while the second consists of medical retinal images. The details of each dataset considered in this research are provided in the following subsections.

3.1. Complicated Natural Images

First, we considered various types of images: dummy face images, natural face images, complex face images in the form of video sequences, and intricate window images. These images exhibit variations and illumination, with dummy images sized at 49×49 pixels, natural face images at 80×60 pixels, video face images at 232×312 pixels, and complicated window images each measuring 512×512 pixels. We evaluated the performance of the proposed method using dummy face images, complex images in the form of video sequences, and the challenging Labeled Faces in the Wild (LFW) dataset [19], which includes images with variations in pose, expression, lighting, and occlusion. The natural face images are sourced from a database, with each image having dimensions of 80×60 pixels. Finally, we conduct an experiment on more complicated face images in videos taken from the Al Gore talking [19]. In this, video, three different video face images with the size 232×312 are considered. Following this, we tested the method on complex, distorted window images sized at 512×512 pixels from [22].

3.2. Medical Retinal Images

Second to verify the performance of the proposed method in medical aspect, we considered several retinal images, from which first the EyeQ [25], consists of $28{,}480$ training and $15{,}128$ testing images, including the high-quality retinal images called ground truth and degraded low-quality images with added artifacts and noises. We selected three retinal images with each image size of 800×800 pixels retinal images from EyeQ for performance assessment through visualization and numerical analysis based on the full and non-full reference categories. The dataset is publicly available at (https://github.com/HzFu/EyeQ). Following this, we considered a synthetic dataset generated by adding salt and pepper noise ($5\%, 10\%, 15\%, 20\%, 25\%$ noise density) to input retinal images (!), introducing white pixels to simulate challenging conditions for image processing algorithms.

Third, we considered the Digital Retinal Images for Vessel Extraction (DRIVE) (https://paperswithcode.com/dataset/drive) dataset for retinal vessel segmentation. Each image resolution is 584×565 pixels with eight bits per color channel (3 channels). It consists of a total of 40 color fundus images. The images were obtained from a diabetic retinopathy screening program in the Netherlands. Thus, we considered three distorted testing images from these images to see the performance of the proposed method as compared with SOTA methods.

Finally, the STARE (Structured Analysis of the Retina dataset) (https://paperswithcode.com/dataset/stare) which primarily used in medical research ophthalmology. These images are often used to evaluate and develop advanced image processing techniques and machine learning models in retinal imaging for automatic detection and classification of retinal diseases such as diabetic retinopathy, macular degeneration, and glaucoma. The STARE dataset includes retinal vessel segmentation. It contains 81 equal-sized 700×605 color retinal fundus images. For each image, two groups of annotations are provided.

The purpose of the datasets is to examine the effectiveness of the proposed method to see the efficiency of the newly developed method, we compared it with SOTAs. To verify the visualization results we also considered three different metrics mainly the PSNR, SSIM and RAE. The formula for each metrics is mentioned in below. The effectiveness of the proposed method is checked through numerical measures using PSNR, which is defined as:

$$PSNR(f,\hat{f}) = 10log_{10}^{\frac{255^2}{\frac{1}{m\times n}\sum_{i=1}^{!}\sum_{i=1}^{n}(f_{ij}-\hat{f}_{ij})^2}} \quad (18)$$

where both the original image f and the recovered image $\hat{f}$ are of size $m\times n$. Similarly, the relative absolute error between the ground truth and recovered images is given by:

$$\text{RAE}(\hat{f},f) = \frac{\|\hat{f}-f\|_1}{\|f\|_1} \quad (19)$$

where $\|\mathbf{X}\|_1 = \sum_{i=1}^{m}\sum_{j=1}^{n}|x_{ij}|$

Moreover, the SSIM between the ground truth and recovered images is given by:

$$\text{SSIM}(f!!\hat{}) = \frac{(2\mu_f\mu_{\hat{f}}+c_1)(2\sigma_{f\hat{f}}+c_2)}{(\mu_f^2+\mu_{\hat{f}}^2+c_1)(\sigma_f^2+\sigma_{\hat{f}}^2+c_2!} \quad (20)$$

4. NUMERICAL EXPERIMENTS

The proposed method is rigorously compared with other SOTAs, including RPCA NNM [13], RPCA WAT [10], RPCA with LRMR [14], and BM2A [23] through image visualization and numerical simulations using the PSNR, SSIM and RAE between the recovered and the original images. Furthermore, the performance of the new method is compared between the ground truth and the recovered images generated by the specified baseline methods. The recovered images are obtained from the degraded images by adding noisy images that combine salt and pepper noise.

4.1. Ablation Studies: Synthetic Retinal Image Data Analysis

First, we generated synthetic noise by combining salt-and-pepper noise to evaluate the performance of adding a log-weighted nuclear norm with the $L_{2,1}$ norm in removing noise from the original retinal images with each having 800×800 pixels retinal images from EyeQ. When we added 5% noise to the original retinal images, as shown in Figure **1**, the log-weighted nuclear norm combined with the $L_{2,1}$ norm outperformed both the classical nuclear norm and the weighted nuclear norm with the L_1 norm. Furthermore, when we add the level of noise from 5% to 15%, the result we attained are given in Figures **1-3**. These findings are consistent with the numerical results presented in Table **1** and **2**. The findings of the study showed that as the noise level increases the performance of the methods with different norms decline but the LWNN with the $L_{2,1}$ norm is relatively better in substantially removing outliers and noises, and enhancing the quality of retinal image analysis as illustrated in Figures **4-6**.

Table 1: PSNR, SSIM, and RAE for each Method Figure 1

Methods	PSNR	SSIM	RAE
RPCA with LWNN + $L_{2,1}$ Norm	42.7863	0.96544	0.024173
RPCA with $L_* + !\ _1$ Norm	17.6445	0.58494	0.29832
RPCA with $L_{!\ ,*}$ + L_1 + τ_i	35.1509	0.94567	0.058323

Table 2: PSNR, SSIM, and RAE for Each Method at 10% Noise Figure 2

Methods	PSNR	SSIM	RAE
RPCA with LWNN + $L_{2,1}$ Norm	36.0213	0.89542	0.06362
RPCA with $L_* + L_1$ Norm	14.6401	0.45326	0.42160
RPCA with $L_{w,*}$ + L_1 + τ_i	34.2208	0.94311	0.07286

These numerical values were obtained by computing between the ground truth and recovered images. From this, we observed that RPCA with the log-weighted nuclear norm (LWNN) and $L_{2,1}$ norm outperforms over RPCA with $L_* + L_1$ Norm and RPCA with $L_{w,*}$ + L_1 + $!\ _i$.

4.2. Natural Face Image Data Analysis

We evaluated our proposed method on the challenging in LFW dataset [19], which includes images

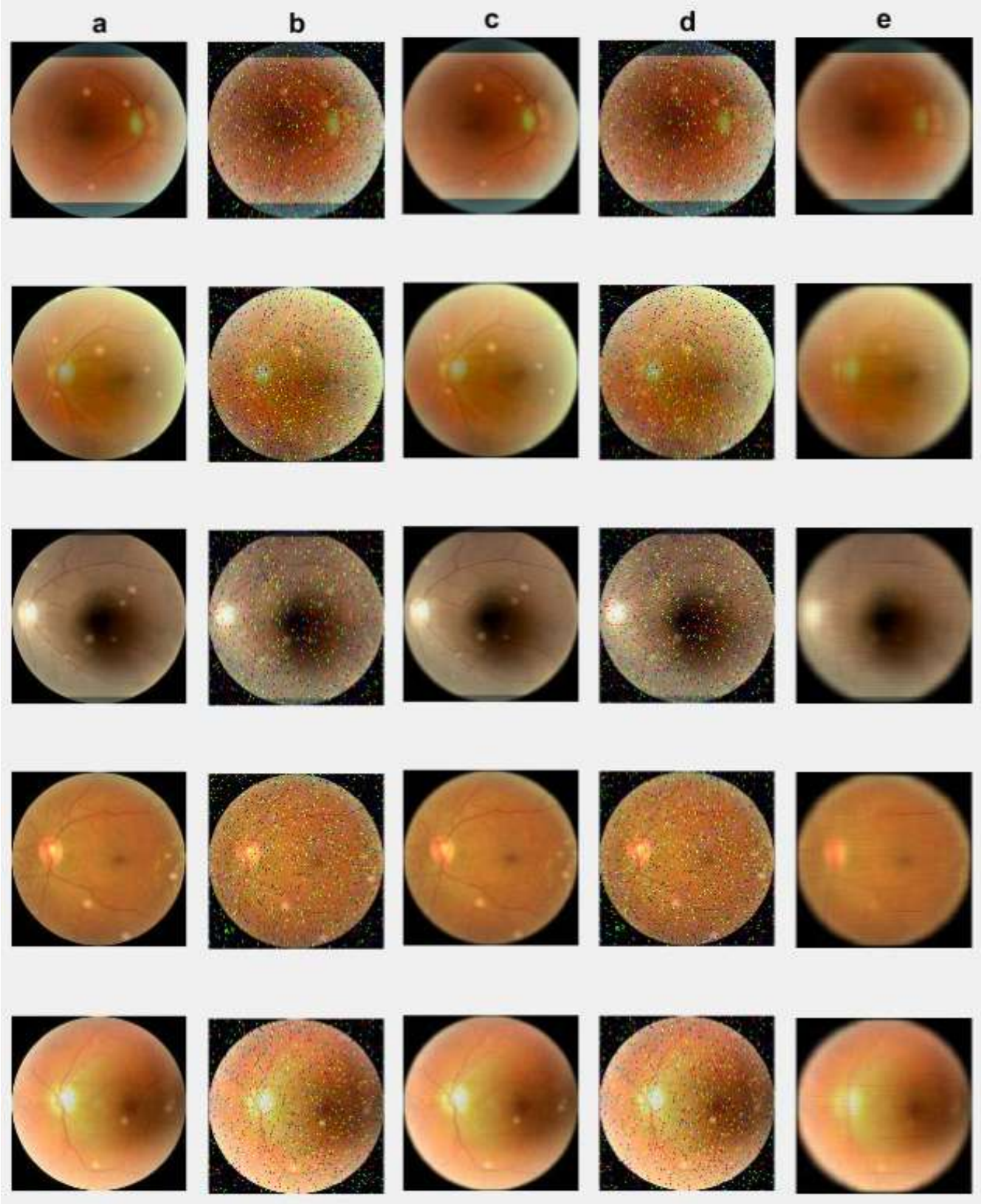

Figure 1: Retinal Image Recovery: a) Original; b) 5% Noise; c) RPCA with LWNN + $!_{2,1}$ Norm; d) RPCA with $L_* + L_1$ Norm; e) RPCA with $L_{w,*} + L_1 + \tau_i$.

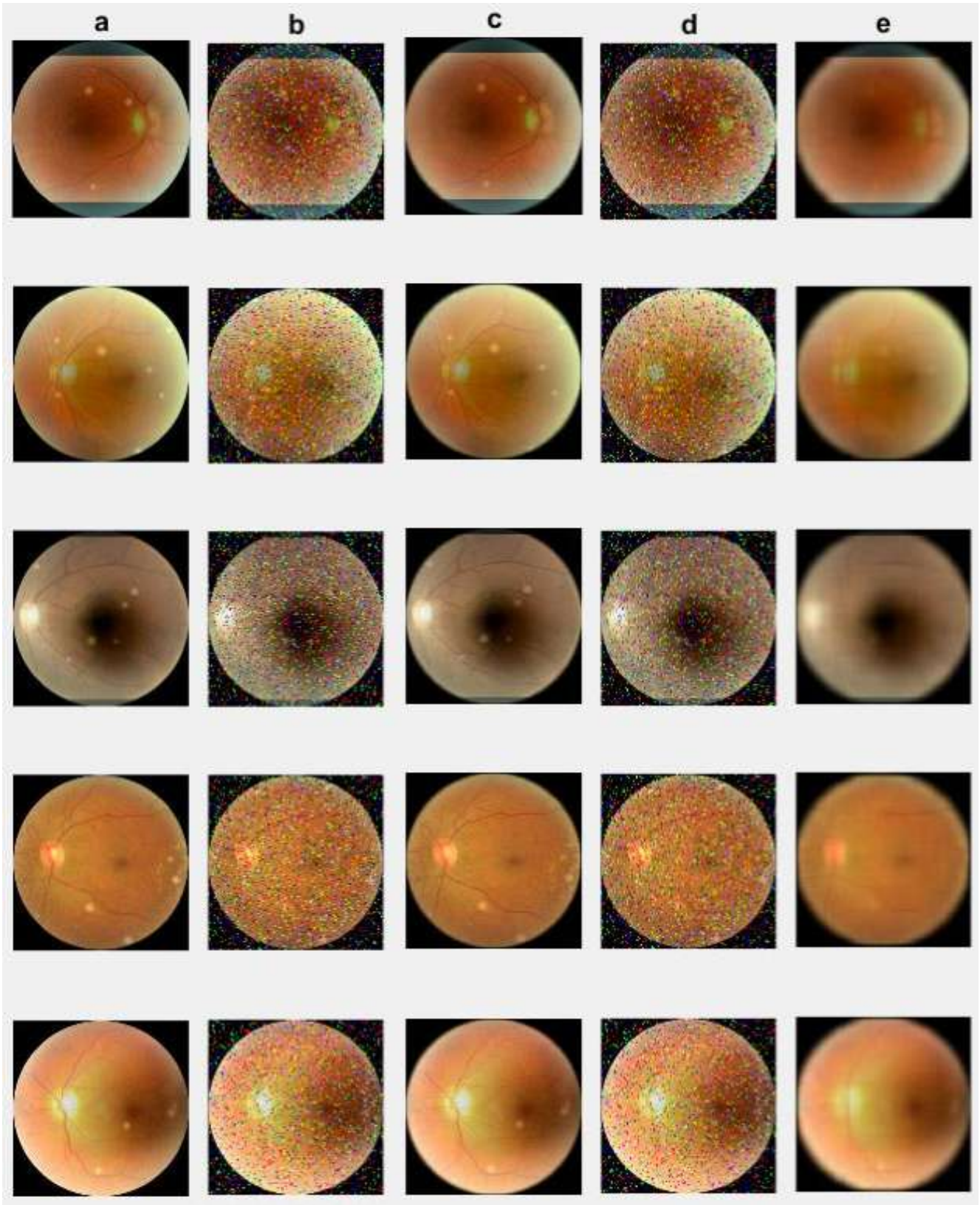

Figure 2: Retinal Image Recovery: a) Original; b) 10% Noise; c) RPCA with LWNN + $L_{2,1}$ Norm; d) RPCA with $L_* + L_1$ Norm; e) RPCA with $L_{w,*}$ + L_1 + τ_i.

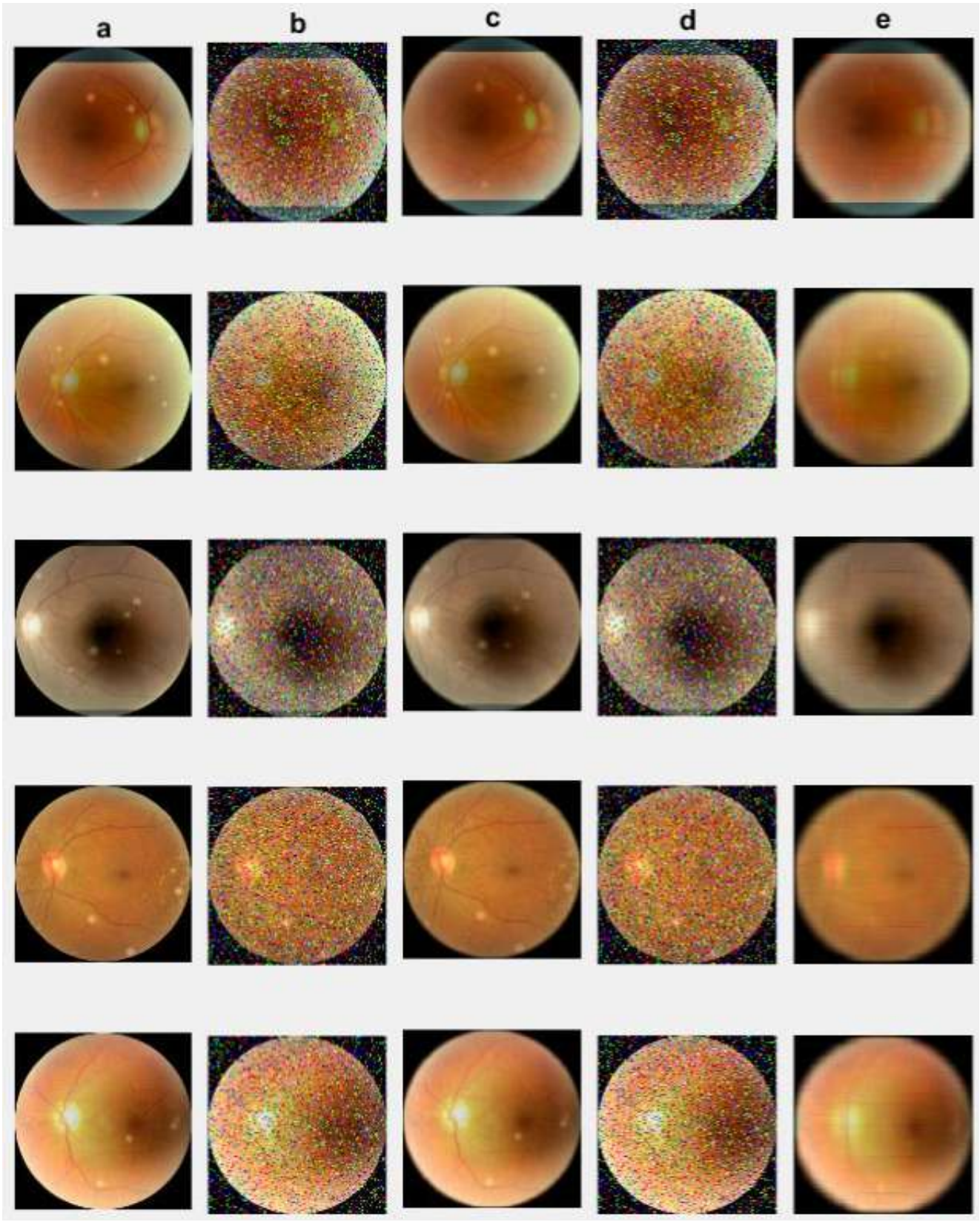

Figure 3: Retinal Image Recovery: a) Original; b) 15% Noise; c) RPCA with LWNN + $L_{2,1}$ Norm; d) RPCA with $L_! + L_1$ Norm; e) RPCA with $L_{w,*}$ + L_1 + τ_i.

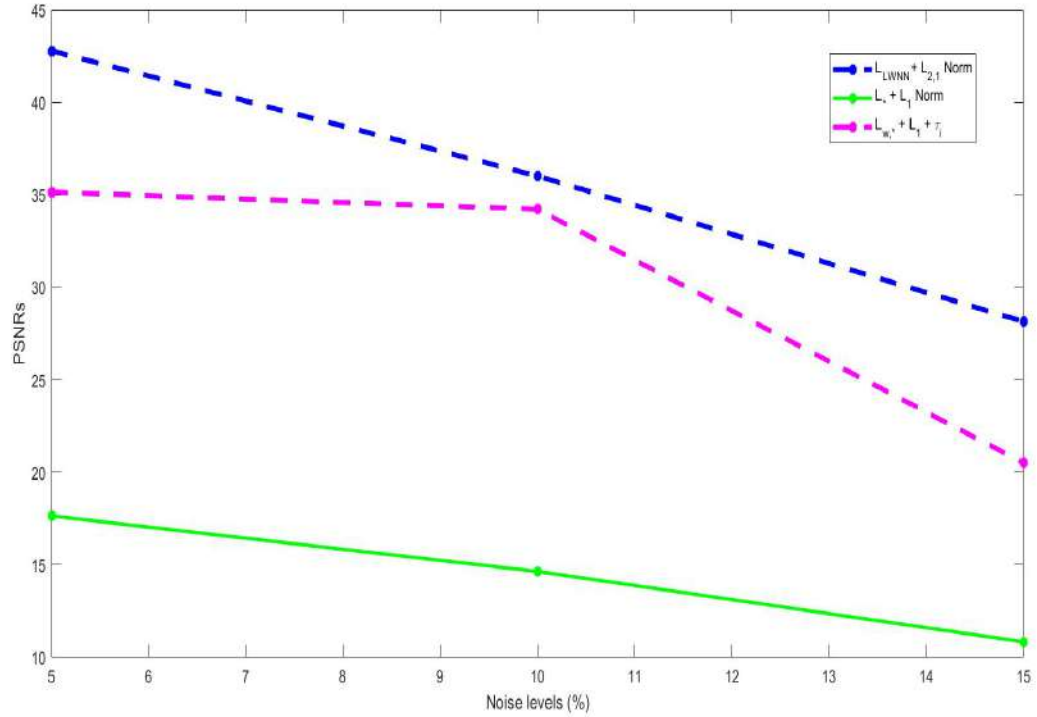

Figure 4: PSNRs versus Noise Levels: RPCA with LWNN + $L_{2,1}$ Norm; RPCA with $L_* + L_1$ Norm; RPCA with $L_{w,*} + L_1 + \tau_i$.

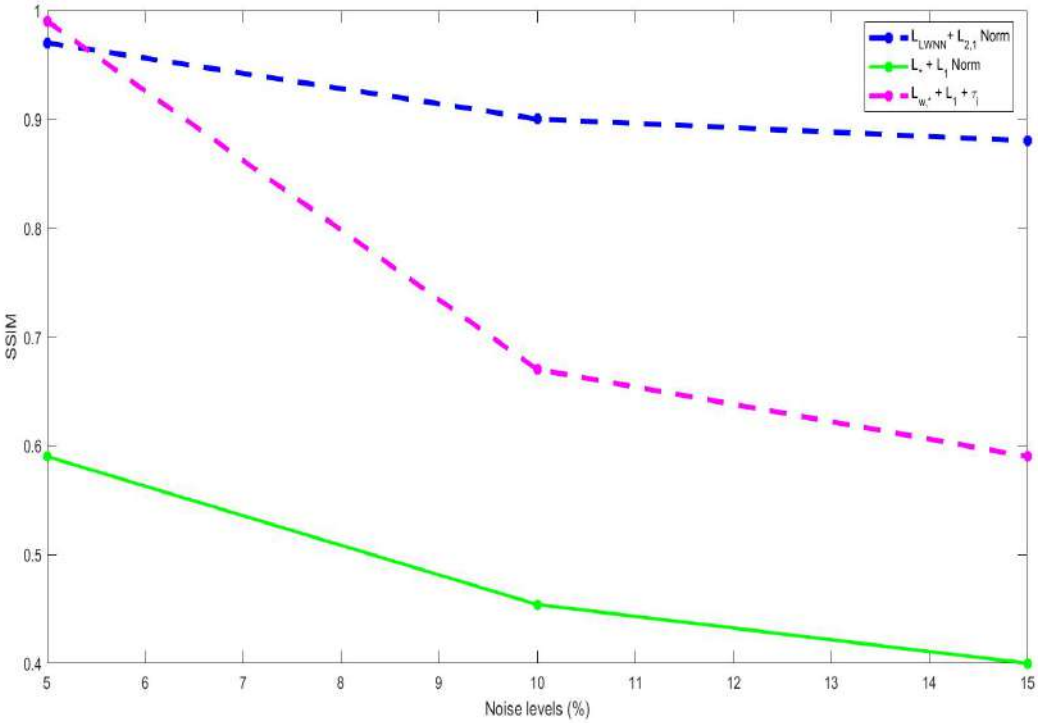

Figure 5: SSIMs versus Noise Levels: RPCA with LWNN + $L_{2,1}$ Norm; RPCA with $L_* + L_1$ Norm; RPCA with $L_{w,*} + L_1 + \tau_i$.

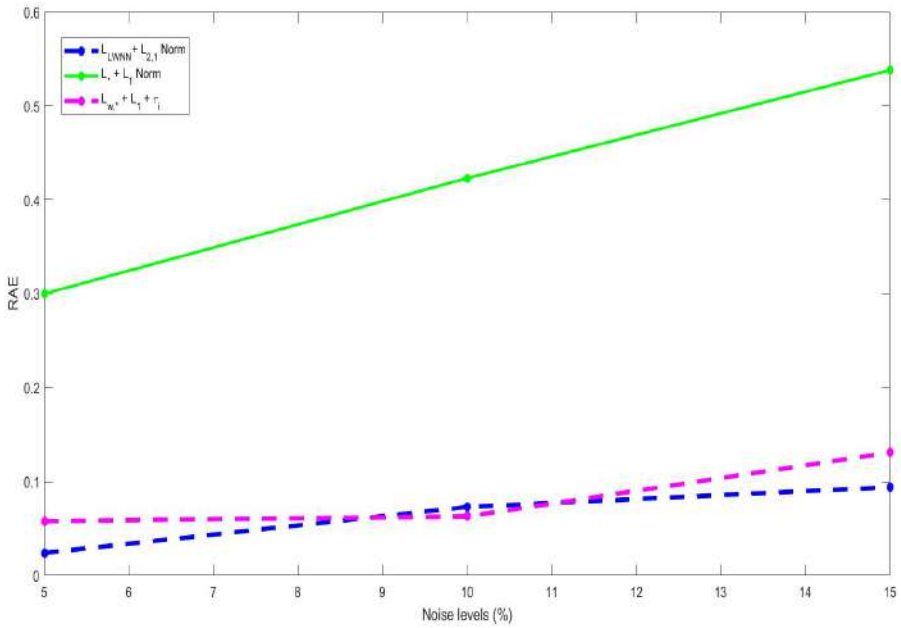

Figure 6: RAEs versus Noise Levels: RPCA with LWNN + $L_{2,1}$ Norm; RPCA with $L_! + L_1$ Norm; RPCA with $L_{w,*}$ + L_1 + τ_i.

Figure 7: Natural Face Image Recovery: a) Degraded; b) Ours; c) RPCA NNM [13]; d) RPCA WAT [10]; e) RPCA with LRMR [14] and BM2A [23].

with variations in pose, expression, lighting, and occlusion. Figure **7** shows the results: starting with the degraded image in Fig. (**7a**), recovered images by our method in Fig. (7b) significantly enhances image quality, outperforming RPCA NNM (c), RPCA WAT (d), RPCA with LRMR (e), and BM2A (f). Our method clearly surpasses SOTAs in complex conditions, as summarized in Table **3**.

4.3. Complicated Image Data Analysis

To verify the performance of our proposed method with the baseline methods, we tested it on complex 512×512 pixels distorted windows taken from [22]. As shown in Fig. **8**, our method delivers clearer visual image quality results, consistent with the numerical simulations in Table **3**. The combination of CLAHE with LWNN in RPCA enhances resilience to noise and outliers. We further validated our method using 100 dummy head images from the CMU Multi-PIE face database and the first three frames of a 140 frame video of Al Gore [19], significantly improving image quality. Our method consistently outperforms state-of-the-art (SOTA) techniques in image recovery, as summarized in Table **3**. The image quality results

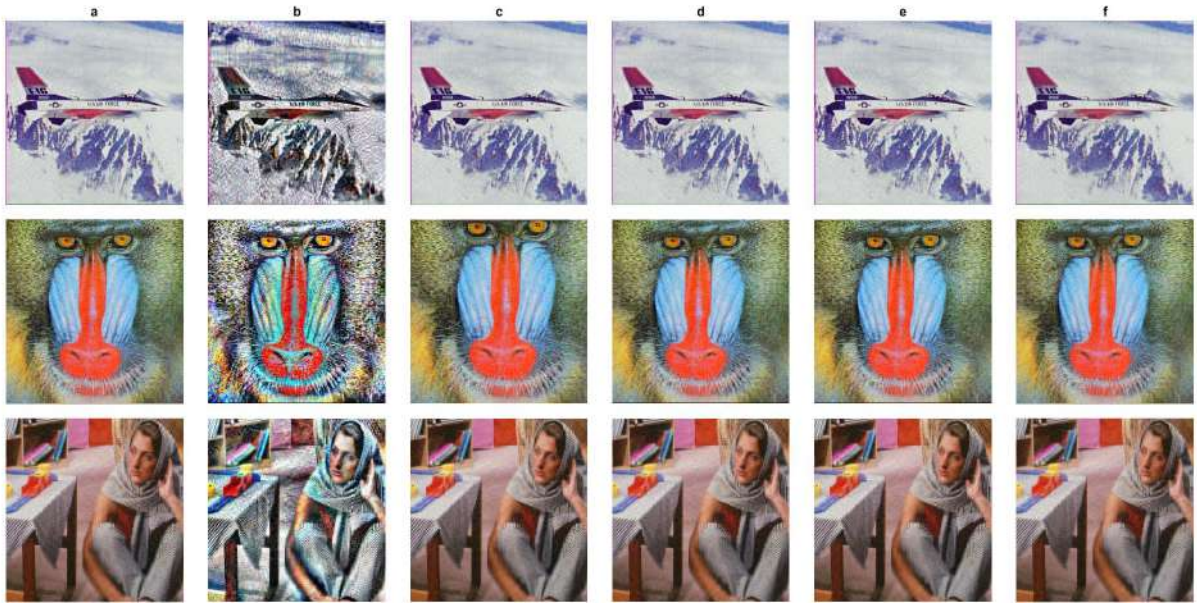

Figure 8: Complicated Window Image Recovery: a) Degraded; b) Ours; c) RPCA NNM [13]; d) RPCA WAT [10]; e) RPCA with LRMR [14] and BM2A [23].

Table 3: Comparison of PSNR, SSIM, and RAE Values for Different Methods across Various Image Types Figs. 7 and 8.

Image Types	Metrics	Ours	RPCA NNM [13]	RPCA WAT [10]	BM2A [23]
Dummy	PSNR	10.61	24.62	26.79	27.57
	SSIM	0.17	0.69	0.75	0.73
	RAE	1.64	0.29	0.23	0.20
Video	PSNR	13.54	22.15	21.00	19.82
	SSIM	0.36	0.62	0.63	0.61
	RAE	0.35	0.14	0.14	0.15
Natural	PSNR	11.57	17.09	16.80	15.68
	SSIM	0.28	0.51	0.52	0.52
	RAE	0.51	0.382	0.38	0.38
Windows	PSNR	10.92	14.81	14.69	14.00
	SSIM	0.23	0.40	0.41	0.42
	RAE	0.62	0.61	0.61	0.60

achieved by the proposed method for the dummy and Al Gore video sequence images are comparable to those of other techniques. We have also included numerical simulations in this paper to support our findings. This is due to we incorporated LWNN and CLAHE along with the $L_{2,1}$ to enhance the quality of images.

4.4. Medical Retinal Image Data Analysis

4.4.1. EyeQ Dataset

Next, we conduct simulations on degraded retinal images taken from the training dataset as in [10]. In this experiment, three degraded retinal images with size 800×800 pixels are considered. As a visualization, some of the improved retinal images based on the above methods are given in Fig. (**9a**), in which our novel method, shown in Fig. (**9b**), better enhances the degraded retinal images as compared to the baseline methods including RPCA NNM [13], RPCA WAT [10], RPCA with LRMR [14], and BM2A [23] from which the results attained by our method is better as compared with the baseline methods. This result resembles the results given in Table **4**, and further verify the effectiveness of the proposed method.

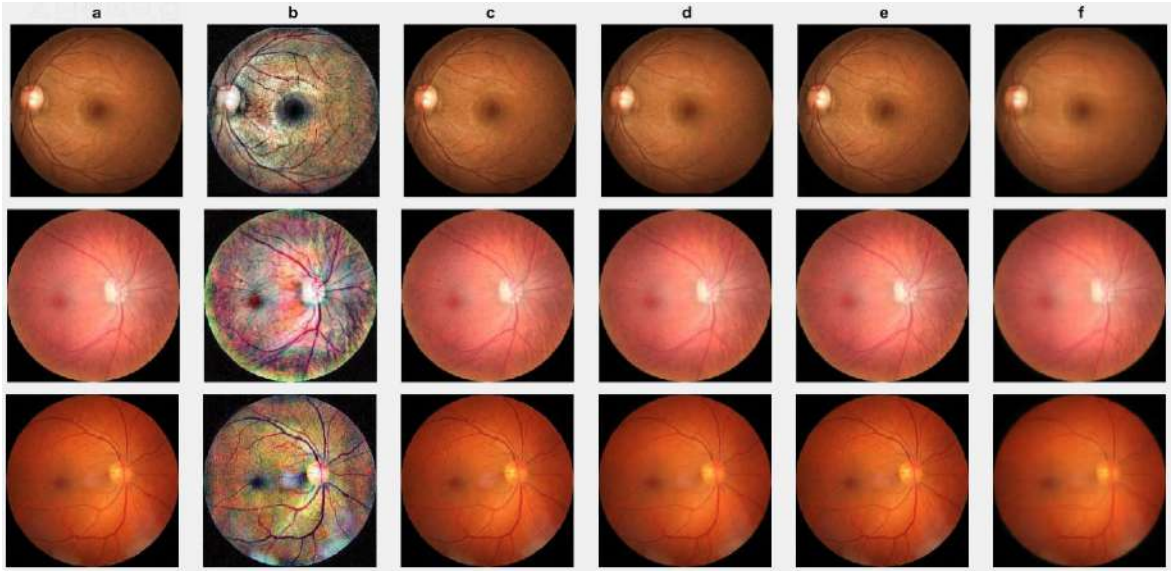

Figure 9: Retinal Image Recovery: a) Degraded; b) Ours; c) RPCA NNM [13]; d) RPCA WAT [10]; e) RPCA with LRMR [14] and BM2A [23].

Similarly, by taking different retinal images from the EyeQ, we achieved similar results which justify incorporating the log weighted nuclear norm along with the $L_{2,1}$ norm in addition to the CLAHE is outperforming to the state of the art methods. The result shown in Figure **10** is more consistent with the results illustrated in the Table **4**.

Table 4: PSNR, SSIM, and RAE for Each Method Figure 9

Methods	PSNR	SSIM	RAE
Ours	14.75	0.21	0.55
RPCA NNM [13]	20.79	0.65	0.31
RPCA WAT [10]	20.70	0.67	0.30
RPCA with LRMR [14]	20.81	0.67	0.33
BM2A [23]	20.10	0.66	0.32

4.4.2. STARE Dataset

To further verify the performance of the proposed method, we also employed our newly developed method on the STARE dataset in which the results are illustrated in Figure **11** and Table **6**.

4.4.3. DRIVE Dataset

To further validate the performance of the proposed method as compared with the baseline methods, we also consider the DRIVE dataset, from which the performance of the proposed method is far better in improving the quality of retinal images. The improved quality attained by the proposed method is given in Fig. **12**, from which this result is more consistent with the results given in Table **7**.

Table 5: PSNR, SSIM, and RAE for Each Method Figure 10

Methods	PSNR	SSIM	RAE
Ours	14.38	0.36	0.68
RPCA NNM [13]	20.97	0.70	0.41
RPCA WAT [10]	20.51	0.71	0.41
RPCA with LRMR [14]	20.96	0.71	0.41
BM2A [23]	19.42	0.68	0.42

Table 6: PSNR, SSIM, and RAE for Each Method Figure 11

Methods	PSNR	SSIM	RAE
Ours	14.06	0.38	0.4517
RPCA NNM [13]	20.34	0.75	0.2684
RPCA WAT [10]	20.37	0.76	0.2662
RPCA with LRMR [14]	20.36	0.76	0.2676
BM2A [23]	20.25	0.77	0.2626

Table 7: PSNR, SSIM, and RAE for each method Figure 12

Methods	PSNR	SSIM	RAE
Ours	17.5306	0.3759	0.3566
RPCA NNM [13]	24.2370	0.8138	0.1685
RPCA WAT [10]	24.2406	0.8211	0.1676
RPCA with LRMR [14]	24.2506	0.8165	0.1682
BM2A [23]	24.0004	0.8295	0.1676

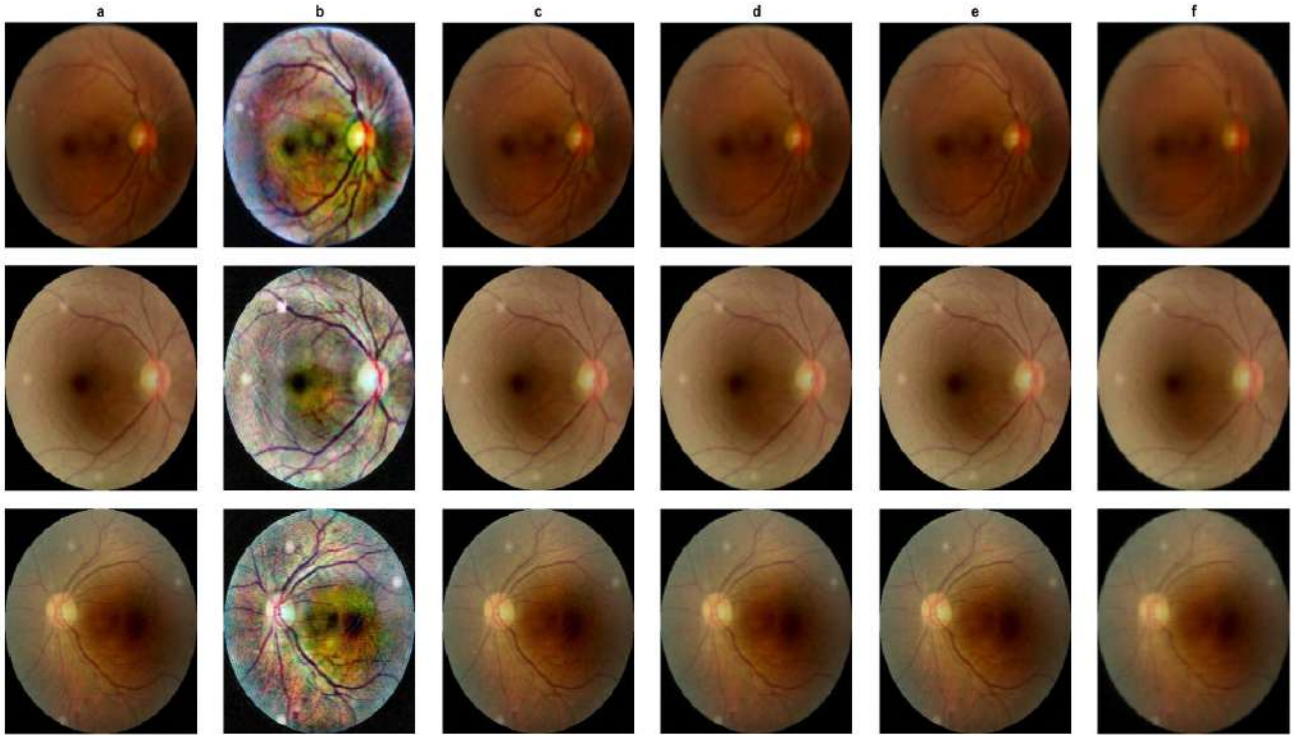

Figure 10: Retinal Image Recovery: a) Degraded; b) Ours; c) RPCA NNM [13]; d) RPCA WAT [10]; e) RPCA with LRMR [14] and BM2A [23]

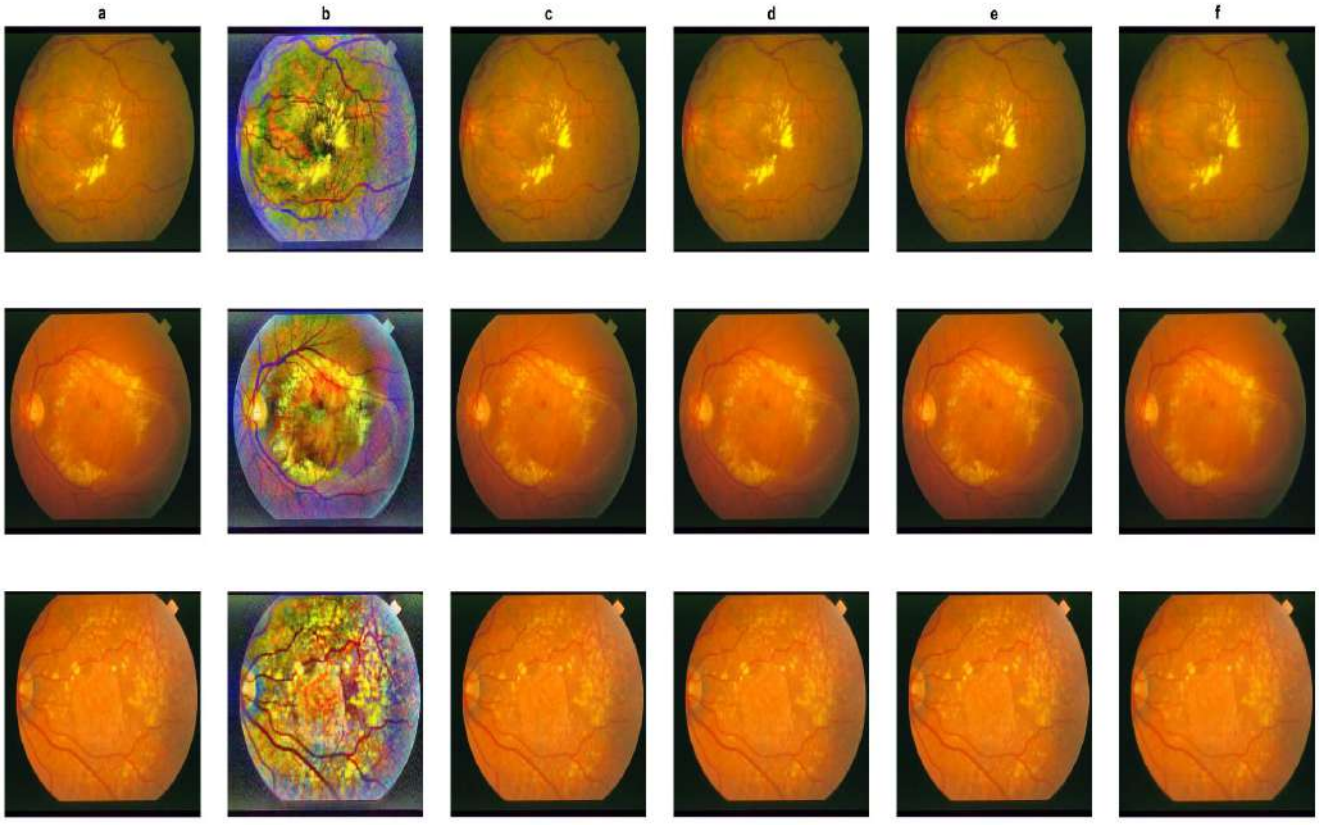

Figure 11: STARE Retinal Image Recovery: a) Degraded; b) Ours; c) RPCA NNM [13]; d) RPCA WAT [10]; e) RPCA with LRMR [14] and BM2A [23].

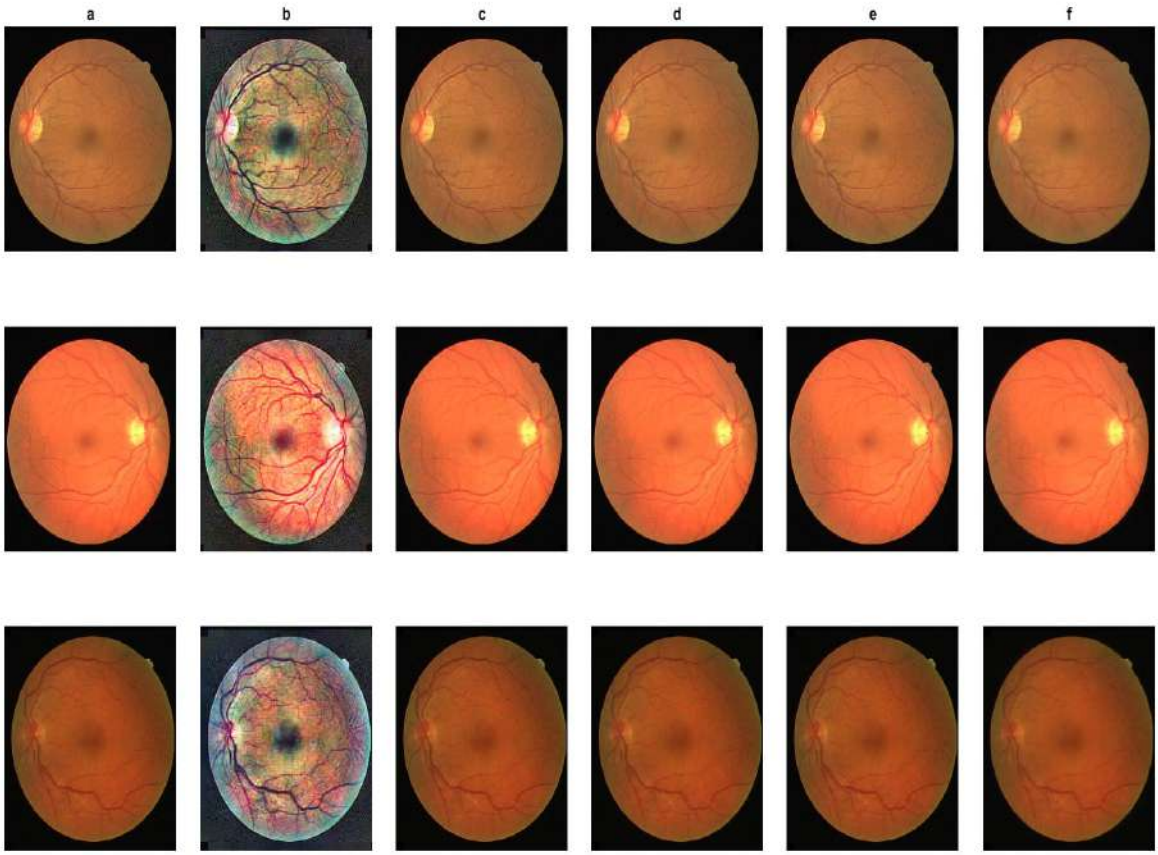

Figure 12: DRIVE Retinal Image Recovery: a) Degraded; b) Ours; c) RPCA NNM [13]; d) RPCA WAT [10]; e) RPCA with LRMR [14] and BM2A [23].

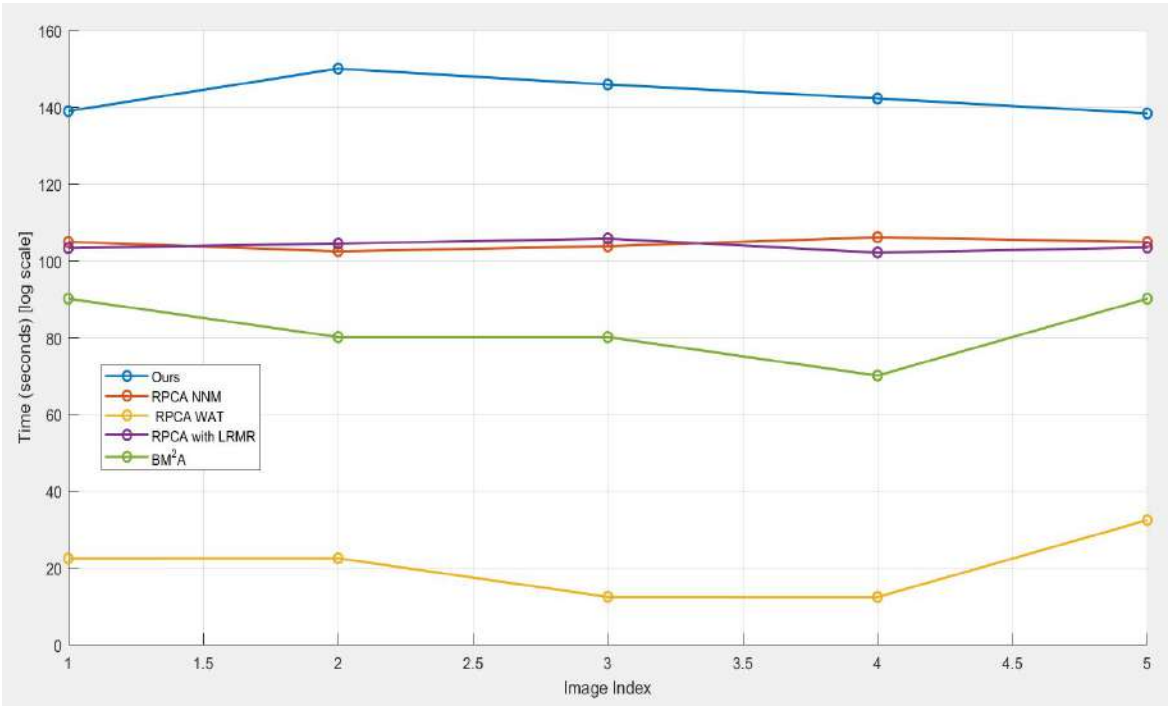

Figure 13: Time Complexity versus Time in Computation.

4.5. Time Complexity

The results of the proposed method, in terms of computational complexity, are compared with state-of-the-art methods using the dataset shown in Figure **13**. The time complexity of the proposed method is higher compared to state-of-the-art methods due to the integration of the Truncated Weighted Nuclear Norm (TWNN) and Adaptive Histogram Equalization (AHE) into the Robust Principal Component Analysis (RPCA) framework. This increased complexity arises because the combination of TWNN and AHE requires additional computations, particularly in handling the weighted nuclear norm and adjusting the image features through histogram equalization. While this process enhances the method's robustness, especially in noise reduction and preserving image details, it also demands more computational resources. Specifically, TWNN focuses on significant singular values for low-rank matrix recovery, and AHE adapts image contrast, both of which involve more intensive matrix operations and parameter adjustments compared to simpler, traditional methods. Therefore, the trade-off between improved performance and increased time complexity should be considered based on the application's requirements for accuracy and efficiency.

5. DISCUSSIONS AND CONCLUSIONS

This work is dedicated to developing a novel method for retinal image enhancement by RPCA method components [11, 12] through combining LWNN with CLAHE and $L_{2,1}$ norm into the pioneering RPCA, aimed at improving their robustness. The development of these approaches represents a significant contribution to the field of computational statistics and data analysis in imaging, particularly in the realm of high-dimensional medical images. Existing methods, as referenced in [11, 12], often lack robustness in the presence of gross noises and outliers within high-dimensional retinal images. In response to this challenge, this article presented a novel method developed to address these issues.

Despite the pioneering RPCA method used for image recovery, several components have been developed. However, their performance in recovering high-dimensional distorted images is not satisfactory for crime detection and clinical diagnosis. Therefore, this paper is proposing a novel RPCA method for improving the quality of highly distorted high dimensional images. The problem is formulated as an optimization problem and the parameters involved are solved via the ADMM approach, our method achieved superior performance compared to SOTAs. A large gap between the recovered and degraded images suggests that the recovery process has substantially improved the image, indicating that the new method has effectively removed distortions or noise and significantly enhanced image quality. One of the major interesting findings of the study show that our method has a closed-form solution, and effective when analyzing large-scale imaging data. In this research, we identified two major findings. First, the combination of LWNN and the $L_{2,1}$ norm is more effective at reducing noise. Second, integrating the LWNN + $L_{2,1}$ norm with CLAHE enhances the details in retinal images that are not visible with existing methods and helps extract the background from natural images. As a future work, we need to incorporate ridge affine transformation to address the misalignment problem and also apply this method in radar imaging to better learn the hidden features.

ACKNOWLEDGEMENTS

This work is partially supported by South Africa National Research Foundation (NRF) and South Africa Medical Research Council (SAMRC) (South Africa DST-NRF-SAMRC SARChI Research Chair in Biostatistics, Grant number 114613).

REFERENCES

[1] Ali AM, Mohammed MA. A comprehensive review of artificial intelligence approaches in omics data processing: evaluating progress and challenges. International Journal of Mathematics, Statistics, and Computer Science 2024; 2: 114-167. https://doi.org/10.59543/ijmscs.v2i.8703

[2] Cand•s EJ, Li X, Ma Y, Wright J. Robust principal component analysis? Journal of the ACM (JACM) 2011; 58(3): 1-37. https://doi.org/10.1145/1970392.1970395

[3] Hawe D, Fernández FRH, O'Suilleabháin L, Huang J, Wolsztynski E, O'Sullivan F. Kinetic analysis of dynamic positron emission tomography data using open-source image processing and statistical inference tools. Wiley Interdisciplinary Reviews: Computational Statistics 2012; 4(3): 316-322. https://doi.org/10.1002/wics.1196

[4] Huang H-H, Yu F, Fan X, Zhang T. A framework of regularized low-rank matrix models for regression and classification. Statistics and Computing 2024; 34(1): 10. https://doi.org/10.1007/s11222-023-10318-z

[5] Huang Y, Wang Z, Chen Q, Chen W. Robust principal component analysis via truncated l_{1 – 2} minimization. In 2023 International Joint Conference on Neural Networks (IJCNN), IEEE 2023; pp. 1-9. https://doi.org/10.1109/IJCNN54540.2023.10191506

[6] Hu W, Pan T, Kong D, Shen W. Nonparametric matrix response regression with application to brain imaging data analysis. Biometrics 2021; 77(4): 1227-1240. https://doi.org/10.1111/biom.13362

[7] Ijaz A, Choi J. Anomaly detection of electromyographic signals. IEEE Transactions on Neural Systems and Rehabilitation Engineering 2018; 26(4): 770-779. https://doi.org/10.1109/TNSRE.2018.2813421

[8] He J, Zhang D, Balzano L, Tao T. Iterative Grassmannian optimization for robust image alignment. Image and Vision Computing 2014; 32(10): 800-813. https://doi.org/10.1016/j.imavis.2014.02.015

[9] Kheddar H, Hemis M, Himeur Y. Automatic speech recognition using advanced deep learning approaches: A survey. Information Fusion 2024; p. 102422. https://doi.org/10.1016/j.inffus.2024.102422

[10] Likassa HT, Chen D-G, Chen K, Wang Y, Zhu W. Robust pca with $l_{w,!}$ and $l_{2,1}$ norms: A novel method for low-quality retinal image enhancement. Journal of Imaging 2024; 10(7): 151. https://doi.org/10.3390/jimaging10070151

[11] Likassa HT, Fang W-H, Chuang Y-A. Modified robust image alignment by sparse and low rank decomposition for highly linearly correlated data. In 2018 3rd International Conference on Intelligent Green Building and Smart Grid 2018; pp. 1-4. https://doi.org/10.1109/IGBSG.2018.8393549

[12] Likassa HT, Fang W-H, Leu J-S. Robust image recovery via affine transformation and l_{2,1} norm. IEEE Access 2019; 7: 125011-125021. https://doi.org/10.1109/ACCESS.2019.2932470

[13] Liu J, Rao BD. Robust pca via regularization. IEEE Transactions on Signal Processing 2018; 67(2): 535-549. https://doi.org/10.1109/TSP.2018.2883924

[14] Liu X, Hou J, Wang J. Robust low-rank matrix recovery fusing local-smoothness. IEEE Signal Processing Letters 2022; 29: 2552-2556. https://doi.org/10.1109/LSP.2022.3229555

[15] Liu Y, Zhang Q, Chen Y, Cheng Q, Peng C. Hyperspectral image denoising with log-based robust pca. In 2021 IEEE International Conference on Image Processing 2021; pp. 1634-1638. https://doi.org/10.1109/ICIP42928.2021.9506050

[16] Li X, Xu D, Zhou H, Li L. Tucker tensor regression and neuroimaging analysis. Statistics in Biosciences 2018; 10(3): 520-545. https://doi.org/10.1007/s12561-018-9215-6

[17] Mejia AF, Nebel MB, Eloyan A, Caffo B, Lindquist MA. Pca leverage: outlier detection for high-dimensional functional magnetic resonance imaging data. Biostatistics 2017; 18(3): 521-536. https://doi.org/10.1093/biostatistics/kxw050

[18] Naiman DQ, Priebe CE. Computing scan statistic p values using importance sampling, with applications to genetics and medical image analysis. Journal of Computational and Graphical Statistics 2001; 10(2): 296-328. https://doi.org/10.1198/10618600152628194

[19] Peng Y, Ganesh A, Wright J, Xu W, Ma Y. Rasl: Robust alignment by sparse and low-rank decomposition for linearly correlated images. IEEE Transactions on Pattern Analysis and Machine Intelligence 2012; 34(11): 2233-2246. https://doi.org/10.1109/TPAMI.2011.282

[20] Pluim JPW, Maintz JBA, Viergever MA. Mutual-information-based registration of medical images: a survey. IEEE Transactions on Medical Imaging 2003; 22(8): 986-1004. https://doi.org/10.1109/TMI.2003.815867

[21] Qin B, Mao H, Liu Y, Zhao J, Lv Y, Zhu Y, Ding S, Chen X. Robust pca unrolling network for super-resolution vessel extraction in x-ray coronary angiography. IEEE Transactions on Medical Imaging 2022; 41(11): 3087-3098. https://doi.org/10.1109/TMI.2022.3177626

[22] Qiu Y, Zhou G, Huang Z, Zhao Q, Xie S. Efficient tensor robust pca under hybrid model of tucker and tensor train. IEEE Signal Processing Letters 2022; 29: 627-631. https://doi.org/10.1109/LSP.2022.3143721

[23] Rajpurohit P, Arora A, Babu P. A block minorization-maximization algorithm for row-sparse principal component analysis. IEEE Signal Processing Letters 2024. https://doi.org/10.1109/LSP.2024.3431463

[24] Sajid H, Cheung S-CS. Universal multimode background subtraction. IEEE Transactions on Image Processing 2017; 26(7): 3249-3260. https://doi.org/10.1109/TIP.2017.2695882

[25] Shen Z, Fu H, Shen J, Shao L. Modeling and enhancing low-quality retinal fundus images. IEEE Transactions on Medical Maging 2020; 40(3): 996-1006. https://doi.org/10.1109/TMI.2020.3043495

[26] Song W, Zhu J, Li Y, Chen C. Image alignment by online robust pca via stochastic gradient descent. IEEE Transactions on Circuits and Systems for video Technology 2015; 26(7): 1241-1250. https://doi.org/10.1109/TCSVT.2015.2455711

[27] Song Y, Li J, Chen X, Zhang D, Tang Q, Yang K. An efficient tensor completion method via truncated nuclear norm. Journal of Visual Communication and Image Representation 2020; 70: 102791. https://doi.org/10.1016/j.jvcir.2020.102791

[28] Verbanck M, Josse J, Husson F. Regularised pca to denoise and visualise data. Statistics and Computing 2015; 25(2): 471-486. https://doi.org/10.1007/s11222-013-9444-y

[29] Wu D, Zhang H, Nie F, Wang R, Yang C, Jia X, Li X. Double-attentive principle component analysis. IEEE Signal Processing Letters 2020; 27: 1814-1818. https://doi.org/10.1109/LSP.2020.3027462

[30] Xu Y, Jasra A. A method for high-dimensional smoothing. Journal of the Korean Statistical Society 2019; 48: 50-67. https://doi.org/10.1016/j.jkss.2018.08.004

[31] Zhou H, Li L, Zhu H. Tensor regression with applications in neuroimaging data analysis. Journal of the American Statistical Association 2013; 108(502): 540-552. https://doi.org/10.1080/01621459.2013.776499

Received on 29-09-2024 Accepted on 27-10-2024 Published on 26-11-2024

https://doi.org/10.6000/1929-6029.2024.13.25